Modeling the Evolution and Life Cycle of Radiative Cold Pools and Fog

TRAVIS H. WILSON AND ROBERT G. FOVELL

Department of Atmospheric and Oceanic Sciences, University of California, Los Angeles, Los Angeles, California

(Manuscript received 30 July 2017, in final form 14 December 2017)

ABSTRACT

Despite an increased understanding of the physical processes involved, forecasting radiative cold pools and their associated meteorological phenomena (e.g., fog and freezing rain) remains a challenging problem in mesoscale models. The present study is focused on California's tule fog where the Weather Research and Forecasting (WRF) Model's frequent inability to forecast these events is addressed and substantially improved. Specifically, this was accomplished with four major changes from a commonly employed, default configuration. First, horizontal model diffusion and numerical filtering along terrain slopes was deactivated (or mitigated) since it is unphysical and can completely prevent the development of fog. However, this often resulted in unrealistically persistent foggy boundary layers that failed to lift. Next, changes specific to the Yonsei University (YSU) planetary boundary layer (PBL) scheme were adopted that include using the ice–liquid-water potential temperature θ_{il} to determine vertical stability, a reversed eddy mixing K profile to represent the consequences of negatively buoyant thermals originating near the fog (PBL) top, and an additional entrainment term to account for the turbulence generated by cloud-top (radiative and evaporative) cooling. While other changes will be discussed, it is these modifications that create, to a sizable degree, marked improvements in modeling the evolution and life cycle of fog, low stratus clouds, and adiabatic cold pools.

1. Introduction

Dense fog, whether over the land or sea, can have large socioeconomic impacts by disrupting travel and jeopardizing public safety (Westcott 2007; Huang et al. 2015). Ten years' worth of data (2004–13) obtained from California's Internet Statewide Integrated Traffic Records System reveal that of the traffic accidents involving weather, only 10% are associated with fog but account for 28% of all weather-related fatalities (CHP 2017). This makes travel in these conditions particularly dangerous, especially during the overnight and early morning hours when it is most widespread and dense. Furthermore, the Federal Aviation Administration (FAA) reports that fog and low clouds account for nearly 18% of their weather-related accidents, second only to wind (Federal Aviation Administration 2010).

Despite its disruptions to travel and impact on public safety, forecasting and modeling fog remains a challenging problem (Westcott 2007; Zhou and Du 2010; Bergot et al. 2007; Steeneveld et al. 2015). The difficulties at least partially stem from the fact that numerous feedbacks in fog can occur, all of which are sensitive to the resolution, initial conditions, and physical parameterizations within the model (Van der Velde et al. 2010; Holtslag et al. 1990; Bergot and Guedalia 1994; Clark and Hopwood 2001; Bergot et al. 2007). Among the parameterizations, the land surface, microphysics, radiation, and boundary layer each play particularly important roles during the formation, maintenance, and eventual demise of fog. Unfortunately, the Advanced Research version of WRF (ARW; Skamarock et al. 2008), along with the fifth-generation National Center for Atmospheric Research (NCAR)–Pennsylvania State University Mesoscale Model (MM5), have failed to reproduce the persistence and structure of stagnant "cold pool" conditions—which are typically associated with radiation fog—despite improvements with respect to horizontal and vertical resolution and to model physics (Baker et al. 2011). For example, Ryerson and Hacker (2014) have demonstrated that the WRF Model was unable to produce fog in California's Central Valley (CV) that was largely traced to an overnight warm bias. This warm bias combined with a notable dry bias in California's CV was also uncovered during stagnant meteorological conditions by Wilson and Fovell (2016). Not surprisingly, it has been suggested that a cold-pool-aware boundary layer

Corresponding author: Prof. Robert Fovell, rfovell@albany.edu

DOI: 10.1175/WAF-D-17-0109.1

and surface schemes may be needed to accurately reproduce such events (Baker et al. 2011; Avey 2011).

It is well accepted that radiation fog forms under clear skies, ample low-level moisture, and light winds as these conditions are conducive to supporting strong surface radiative cooling. This cooling can be enhanced by sheltering from terrain and nearby trees that effectively reduces vertical mixing near the earth's surface (Gustavsson et al. 1998). Given adequate cooling and moisture, near-surface conditions may reach saturation and condensation can begin. During this stage, the radiative flux divergence at the surface dominates the cooling process and supports the initial growth of fog droplets. However, as the number of fog droplets increases and the layer becomes more optically thick, longwave cooling at the surface is dominated by the upwelling longwave radiation by the fog droplets themselves (Haeffelin et al. 2010). This allows fog droplets to become the dominant cooling mechanism, via radiational cooling, while surface cooling effectively shuts off (Zhou and Ferrier 2008).

It has been shown that with sufficient fog-top longwave divergence, the upper part of a fog layer can destabilize (Bergot et al. 2007). With time, the destabilization can continue until nearly the entire fog profile is moist adiabatic (Holets and Swanson 1981; Boers et al. 2013). This creates atmospheric conditions quite similar to stratocumulus-capped planetary boundary layers (PBLs) where cloud-top cooling via radiative flux divergence and cloud droplet evaporation can influence mixing and entrainment (Nicholls and Turton 1986). Certainly, entrainment is well understood to assist with the *dissipation* of fog as it originates not only from fog-top cooling, but also from overshooting surface thermals formed by surface heating. This entertainment and heating is why fog "burns off," or at least thins during the daytime hours.

Modeling fog remains a challenging problem, although it is likely not due to our lack of understanding of the relevant physical mechanisms. In this study, we will argue that some of the important physical processes just discussed are often missing in model parameterizations while some commonly employed options are unphysical and detrimental to the formation of fog itself. We will examine both idealized and real-data cases to understand why and address current problems with the WRF Model while developing new and substantially improved solutions.

The structure of this paper is as follows. Section 2 describes our methodology, our results are presented in section 3, and our conclusions are presented in section 4.

2. Methodology

Using ARW version 3.5.1 (with modifications), radiation fog in the CV will be modeled in both real-data and idealized settings; the latter will be described when introduced. The real-data model setup includes a triply nested design with horizontal resolutions of 36, 12, and 4 km (Fig. 1), although some simulations will not employ the innermost domain. These experiments will use 62 vertical levels that have been adjusted to include 19 full sigma levels in the lowest 1 km above ground level (AGL). This differs from the default settings for real-data WRF simulations that fix the first eight levels (roughly the lowest kilometer) to constant values regardless of the number of vertical grid points chosen. In Wilson and Fovell (2016), we demonstrated how and why increasing the vertical resolution near the surface can beneficially impact humidity forecasts in the CV.

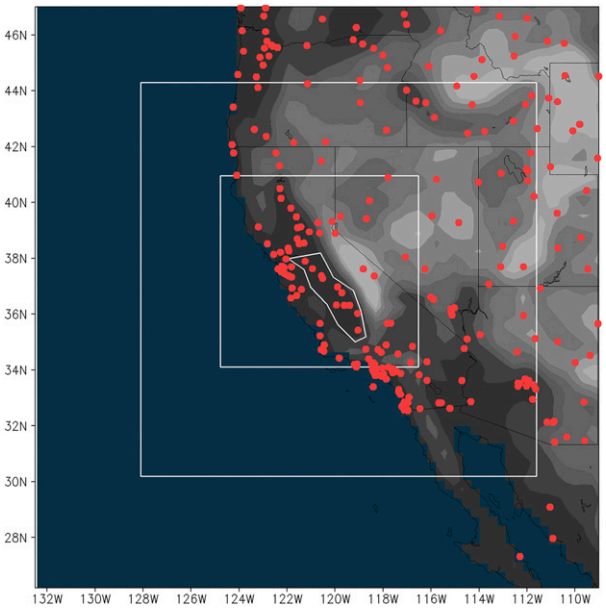

FIG. 1. The 36-, 12-, and 4-km domains used throughout all simulations are shown along with terrain shading derived from the outermost grid. The red dots represent surface ASOS or AWOS stations used to verify the model while the white polygon encloses stations used in the SJV subset.

Our model physics suite includes the WRF double-moment, 5-class (WDM5) microphysics (Lim and Hong 2010), the new Goddard radiation (Chou and Suarez 1999), the Yonsei University (YSU) planetary boundary layer scheme (Hong et al. 2006), and the Noah land surface model (LSM; Ek et al. 2003) in all three domains (see Table 1). The Kain–Fritsch (Kain 2004) cumulus parameterization was active in domains 1 and 2 only. The optional gravitational settling for cloud droplets is activated,[1] as it has been shown to be of importance

[1] Our bug fix that was incorporated into WRF since version 3.6 is employed in our simulations.

TABLE 1. Model physics information.

Physics	Real-data cases		Idealized	
	Default (Figs. 2 and 3)	Recommended (Figs. 10–12)	LES	Coarse grid
Microphysics	WDM5	WDM5	WDM5	WDM5
LSM	Noah	Noah	Noah	Noah
PBL	YSU	Modified YSU	Off	YSU vs modified YSU
Radiation	New Goddard	New Goddard	New Goddard	New Goddard
Horizontal diffusion	Along model surfaces (diff_opt = 1, but off for Fig. 3c)	Off (diff_opt = 0)	In physical space (diff_opt = 2)	In physical space (diff_opt = 2)
K option	2D deformation (km_opt = 4)	2D deformation (km_opt = 4)	3D TKE (km_opt = 2)	2D deformation (km_opt = 4)
Sixth-order filter	Off (except on in Fig. 3c)	Off	Off	Off

when modeling fog cloud water concentrations (Bergot et al. 2007). The Chen and Zhang (2009) modification to the thermal roughness length evaluated by Wilson and Fovell (2016) in the CV is not used. As recommended for real-data cases, our default configuration includes horizontal diffusion computed along model surfaces (diff_opt = 1, km_opt = 4) although, as in Wilson and Fovell (2016), this will be shown to have a significantly negative impact on the simulations. Our default setup does not employ the available sixth-order horizontal filter, which can be used to remove small-scale features, but this option will be evaluated.

The three simulation periods are 29 December 2008–2 January 2009 and 4–7 and 13–16 January 2011. All were dominated by high pressure in the Great Basin and included episodes during which the San Joaquin valley and a large portion of the Sacramento valley were inundated by fog and/or low stratus clouds. We chose to initialize the first event with the ECMWF interim reanalysis (ERA-Interim) and the other two with the North American Regional Reanalysis (NARR). The location, spatial extent, and longevity of low clouds forecasted by the WRF Model are very sensitive to model initialization and forecast lead time, and our selections yielded the best reconstructions of these events with the default model configuration (see Table 2). That said, it will be shown that all of these default runs have significant deficiencies.

Verifications of the weather reconstructions have been performed principally with the Model Evaluation Tools (MET) software, maintained by the Developmental Testbed Center at NCAR, utilizing hourly surface observations from Automated Weather Observing System (AWOS) and Automated Surface Observing System (ASOS) stations (identified in Fig. 1 with red dots) obtained from the Meteorological Assimilation Data Ingest System (MADIS). Comparisons were accomplished by interpolating model fields to the station locations. As our focus is on CV fog, however, we will concentrate on the sites located within the white polygon, the "San Joaquin valley (SJV) subset," which consists of 10 or 11 stations, depending on the event.

3. Results

a. *The December 2008–January 2009 episode: Observations and default simulation*

The red curves in Fig. 2a represent 2-m temperature (solid) and dewpoint (dotted) observations averaged over the San Joaquin valley subset for the period from 29 December 2008 to 2 January 2009. Figure 2b reveals both the number of SJV stations reporting ceiling heights below 1000 m (dashed red curve, axis at right), as well as the ceiling height averaged over just those low-ceiling stations (solid red curve, axis at left). During the first half of the period, subset-averaged dewpoint depressions became small only at night. Early on 30 December, for example, the number of stations reporting sub-1-km ceilings peaked at 9 of 11 around sunrise (about 0730 local time or 1530 UTC), and the average ceiling height at those sites was ≈400 m.

However, starting with sunset on 30 December (about 1700 local time or 0100 UTC 31 December), the number of stations reporting low ceilings rose, eventually reaching all 11 SJV locations, while their average ceiling heights dropped to near zero. (It should be noted that ASOS stations often report a ceiling of 30 m, and rarely 0 m, when fog is observed.) During this interval, fog began spreading across the San Joaquin valley, as evidenced by the visual satellite image for 1800 UTC 31 December (Fig. 3a). Subsequent to that time, the average ceiling height among the SJV stations began to rise, indicating that the fog had begun lifting. Therefore, for much of this period, which extends beyond the final time depicted, the valley could be described as having experienced extensive low stratus rather than fog.

TABLE 2. Case study initialization details.

Case	Simulation period	Initialization time (UTC)	Source
1	29 Dec 2008–2 Jan 2009	1200	ERA-Interim
2	4–7 Jan 2011	0000	NARR
3	13–16 Jan 2011	1200	NARR

Now we turn to the WRF simulation employing the default configuration described in the previous section, made using only the outer two (36 and 12 km) domains. The SJV-averaged 2-m temperature for this simulation (shown in dark blue in Fig. 2a) reveals a diurnal cycle that was unimpacted by clouds because, in fact, no clouds formed within the San Joaquin valley subset at all. The lone exception was the single hour (1300 UTC 30 December, identified with the black arrow in Fig. 2b) during which one station had a simulated cloud ceiling of about 100 m. At 1800 UTC 31 December, the San Joaquin valley was cloud free, although ostensibly realistic low and high clouds appeared in other parts of the domain (Fig. 3b). The lack of low cloud cover led to substantial overpredictions of the 2-m temperature in the SJV during the daylight hours of 31 December and 1 January (as well as some underprediction at night). The inclusion of the 4-km nest improved the simulation as horizontal diffusion errors were lessened, which allowed the fog to be better resolved. This result was expected as similar findings were also noted by Billings et al. (2006). However, the diffusion errors were not eliminated; it is for this reason we will continue to explore the effects of diffusion using the two-domain setup in the following subsection.

b. *Influence of horizontal diffusion on low clouds*

In most real-data applications, the WRF Model is configured such that subgrid-scale mixing in the vertical (even in the free atmosphere) is accomplished via the PBL scheme, leaving horizontal diffusion to be handled via the diff_opt option. As noted earlier, the recommended setting, diff_opt = 1, computes horizontal diffusion along model surfaces, which is problematic in regions of complex terrain, as it can cause unrealistic transport up and down mountain slopes (Billings et al. 2006; Zängl 2005; Wilson and Fovell 2016). Wilson and Fovell (2016) demonstrated that this horizontal mixing forces dry air down into the CV, resulting in a substantial underprediction of near-surface relative humidity. Another diffuser that operates on model surfaces is the sixth-order filter (diff_6th_opt), which targets short-wavelength features and is controlled by the nondimensional coefficient diff_6th_factor.

In this case, both horizontal diffusers act to limit fog formation in the Central Valley. Recall that diff_opt = 1 resulted in a cloud-free CV (Fig. 3b), leading to overprediction of the 2-m temperature during the latter half of the period (Fig. 2a). Deactivating this mixing (diff_opt = 0) but employing the monotonic and positive-definite version of the sixth-order filter (diff_6th_opt = 2) instead

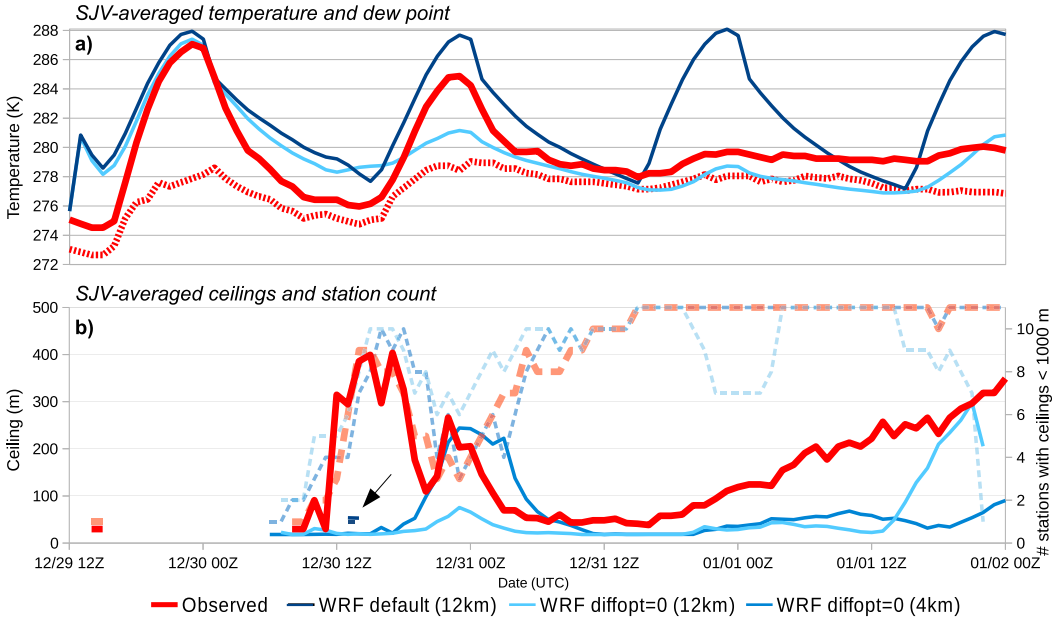

FIG. 2. (a) Observed (red) and simulated (blue) temperatures (solid line) and dewpoints (dotted line) for the SJV subset from 29 Dec 2008 to 2 Jan 2009. (b) Over the same area, the numbers of observed and forecasted stations with ceilings less than 1000 m (dotted line) are shown along with the subsequent ceiling heights (solid line). For simplicity, forecasted dewpoints and results from the 4-km run are not shown in (a).

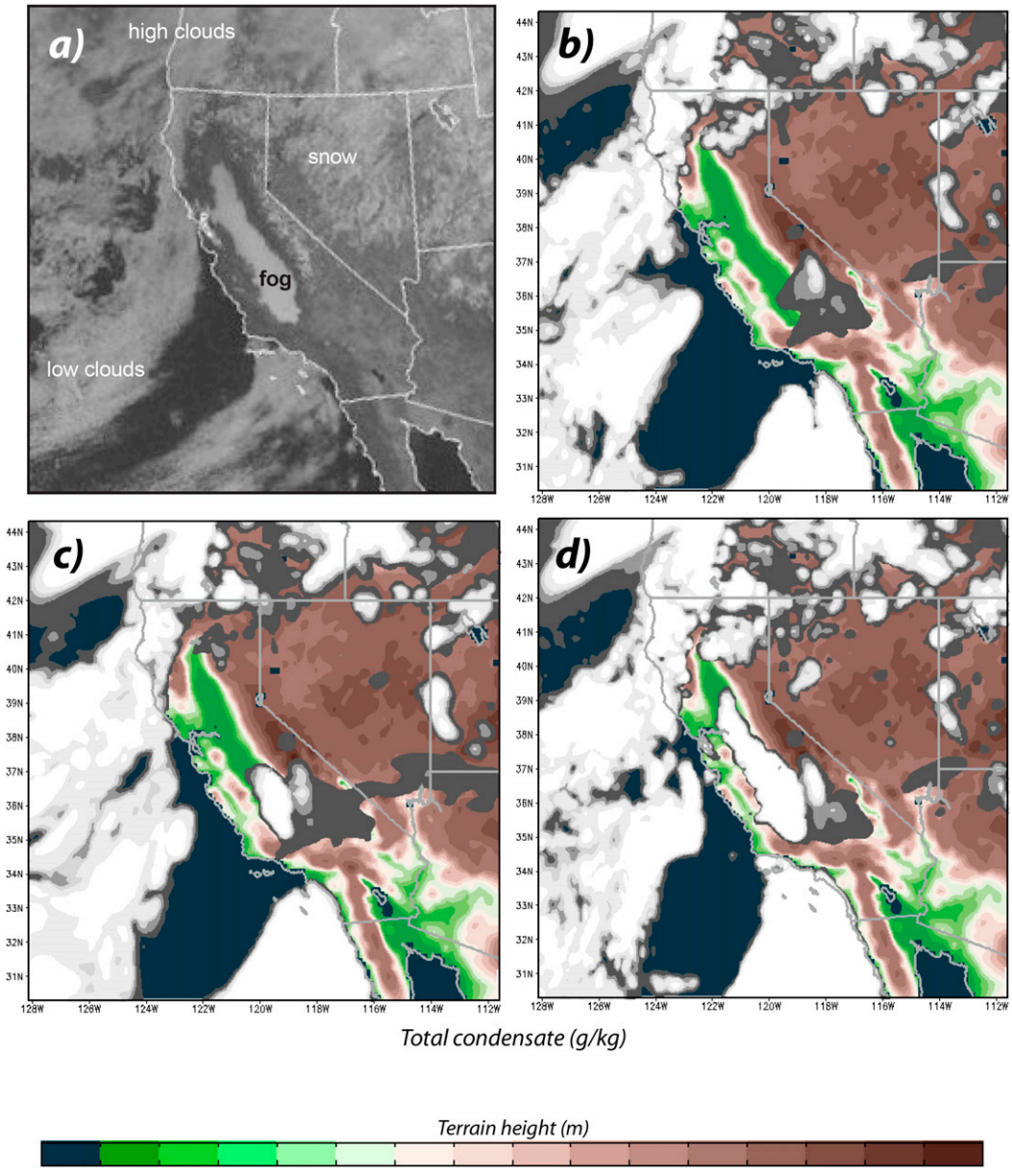

FIG. 3. (a) Visible satellite image for 1800 UTC 31 Dec 2008 along with simulated total-column condensate fields using (b) the default configuration of horizontal diffusion on model surfaces (diff_opt = 1) and no sixth-order filter, (c) no horizontal diffusion (diff_opt = 0) but with a monotonic and positive-definite sixth-order filter (diff_6th_opt = 2) with the typical setting of diff_6th_factor = 0.12, and (d) no horizontal diffusion and no sixth-order filter. These simulations were made without the 4-km innermost nest.

permitted the development of some cloudiness in the southern end of the SJV (Fig. 3c), an incremental improvement.[2] However, removing *both* sources of horizontal mixing along model surfaces allowed substantially more fog development through the Central Valley (Fig. 3d). At least at the time shown, the spatial extent of the cloudiness was comparable to the observations (Fig. 3a), and the patterns of evolution of both 2-m temperatures and low cloud ceilings through the simulation period were somewhat more reasonable (light blue lines on Figs. 2a,b). Beyond the SJV, one can observe that

[2] In this situation, we found that the monotonic and positive-definite version of the filter, which is the recommended option, erodes fog more severely than the alternative (neither positive definite nor monotonic).

the low cloudiness off the southern California coast was also more realistic when horizontal mixing is neglected, with the stratus deck abutting the coastline, as was observed (Figs. 3a,d).

Examination of a number of events supports the general conclusion that horizontal mixing along model surfaces can inhibit fog formation in the CV and, thus, should be avoided in favor of diffusion operating in physical space (i.e., diff_opt = 2) if available.[3] Yet, solving that problem has exposed another: *once the fog forms, the model has a very difficult time getting it to lift*. Recall that while observed ceiling heights began to rise after 1800 UTC 31 December, simulated ceilings remained close to the lowest scalar level about 18 h longer (Fig. 2b). That was in the simulation without the 4-km domain. With that innermost nest active, the fog persisted even longer (dark blue line in Fig. 2b), resulting in an even more substantial low-ceiling bias.

This low-ceiling bias in this area also appears to be a persistent characteristic of WRF simulations that was masked by unrealistic diffusion along terrain slopes. Through extensive testing, we have determined that the bias is largely independent of resolution and initialization (including sources and timing), and thus it appears to be a model physics issue. Unfortunately, fog is an extremely complicated phenomenon and depends on a number of physics packages in the WRF Model including, but not limited to, the microphysics, radiation, PBL, and LSM schemes. Therefore, in order to explore this tightly coupled system in a more controlled setting, we elected to pursue the idealized, large eddy simulations (LESs) of the foggy boundary layer with WRF as described in the next subsection.

c. *Large eddy simulations and comparison with the standard YSU scheme*

The goal of these LES experiments was to directly simulate the boundary layer evolution that PBL schemes like YSU are attempting to capture in coarser-resolution experiments. As a consequence, the other model physics choices (WDM5 microphysics, new Goddard radiation, and the Noah LSM; see Table 1) from our prior runs were retained to enhance comparability, and the model was initialized using a representative sounding (including soil information) from the Central Valley derived from the NARR reanalysis during fog episodes (Fig. 4). This profile was given some supersaturation in the lowest 150 m to permit the rapid development of boundary layer clouds. The doubly periodic domain had 30 grid points in each horizontal direction with 33-m grid spacing. Previous LES studies of cloud-capped PBLs have used domains of 3–5 km in width (Rao and Agee 1996; Khairoutdinov and Kogan 2000); we found no material sensitivity to horizontal domain widths up to 4 km (not shown), likely because of the relatively calm conditions. The vertical grid was stretched, with 101 levels beneath the 12-km model top, of which 38 were in the lowest kilometer, putting the lowest scalar level at 16 m AGL. Spurious inversion-level oscillations of the type reported by Yamaguchi and Feingold (2012) and explained in Xiao et al. (2015) were not observed, likely because of the relatively small moisture change across the inversion in our case.

For the radiation scheme, a typical CV latitude, longitude, and wintertime solar elevation (16 January) were specified and were called every time step (3/10 s). Simulations were started at 0000 UTC, which was just before local sunset, and integrated for 48 h. Although initialized with horizontally homogeneous fields, the development of three-dimensionality was assured via use of the stochastic kinetic energy backscatter scheme (SKEBS; Shutts 2005; Berner et al. 2011).

Figure 5a presents a time versus height field of domain-averaged cloud water content for the control LES experiment. In response to the environment's initial supersaturation, clouds appeared immediately and mixing ratios quickly exceeded $1\,\mathrm{g\,kg^{-1}}$. While the cloud-topped boundary layer continued deepening for the remainder of the simulation, note that the fog lifted into stratus after about 16 h, or about a half-hour after sunrise. The subsequent evolution of the cloud deck was only modestly influenced by the diurnal cycle, thinning but not dissipating during the afternoon, likely owing to the low sun angle during January and the attenuation of solar radiation by the low clouds.

The lifting of the fog into low stratus occurred in the LES simulation because the model was able to rather quickly establish a vertically extensive well-mixed layer. At the initial time, the atmosphere was stably stratified, as confirmed by the fairly steep near-surface vertical gradient of the domain-averaged ice–liquid-water potential temperature θ_{il} field shown in Fig. 6. The ice–liquid-water potential temperature (cf. Betts 1973) can be written as

$$\theta_{il} = \frac{1}{\Pi}\left(T - \frac{L_v q_c}{c_p} - \frac{L_s q_i}{c_p}\right), \tag{1}$$

[3] As noted by Wilson and Fovell (2016), diff_opt = 2, which computes horizontal diffusion in physical space, now (as of WRF version 3.6.1) deactivates mixing where the terrain gradients are large to avoid numerical instability but, as in that study, our results with diff_opt = 2 are indistinguishable from when diff_opt = 0 is employed.

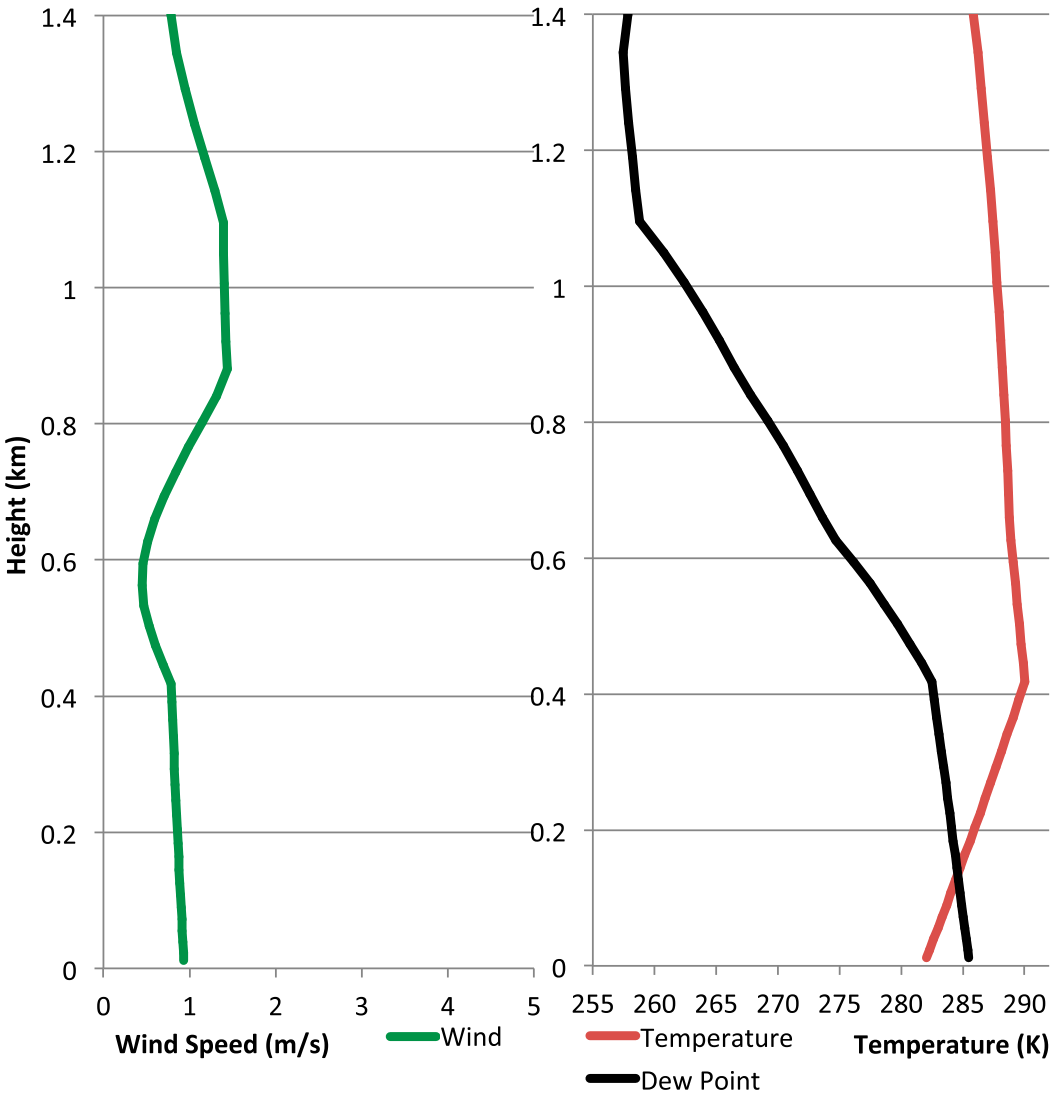

FIG. 4. The initial sounding used for both the LES and coarse-grid idealized simulations.

where Π is the Exner function; T is temperature; L_v and L_s are the latent heat of vaporization and sublimation, respectively; q_c and q_i are the cloud water and ice mixing ratios; and c_p is the heat capacity at constant pressure for dry air.[4] In the absence of cloud water and ice, the ice–liquid-water potential temperature is equal to the potential temperature. However, when cloud water and ice are present, the ice–liquid-water potential temperature removes the heat associated with condensation and deposition, effectively creating a zero vertical gradient for both moist- and dry-adiabatic profiles.

[4] This formula is sufficiently accurate for shallow convection (cf. Bryan and Fritsch 2004).

In Fig. 6, note that the vertical gradient of the ice–liquid-water potential temperature vanished below 200 m AGL by 2 h after initialization, and that this transition toward neutral stratification occurred entirely during the *nighttime* hours. In this case, we are dealing with a moist-adiabatic profile. As one would expect, the surface temperature was decreasing after initialization owing to surface longwave cooling, which in isolation was making the vertical profile more stable. Yet, as the fog thickened overnight, the surface cooling ceased while the cooling at the fog-layer top continued to destabilize the cloudy layer.

This resulted in the establishment of a well-mixed foggy layer that was already 300–400 m deep before sunrise. Further mixed-layer growth was driven by the

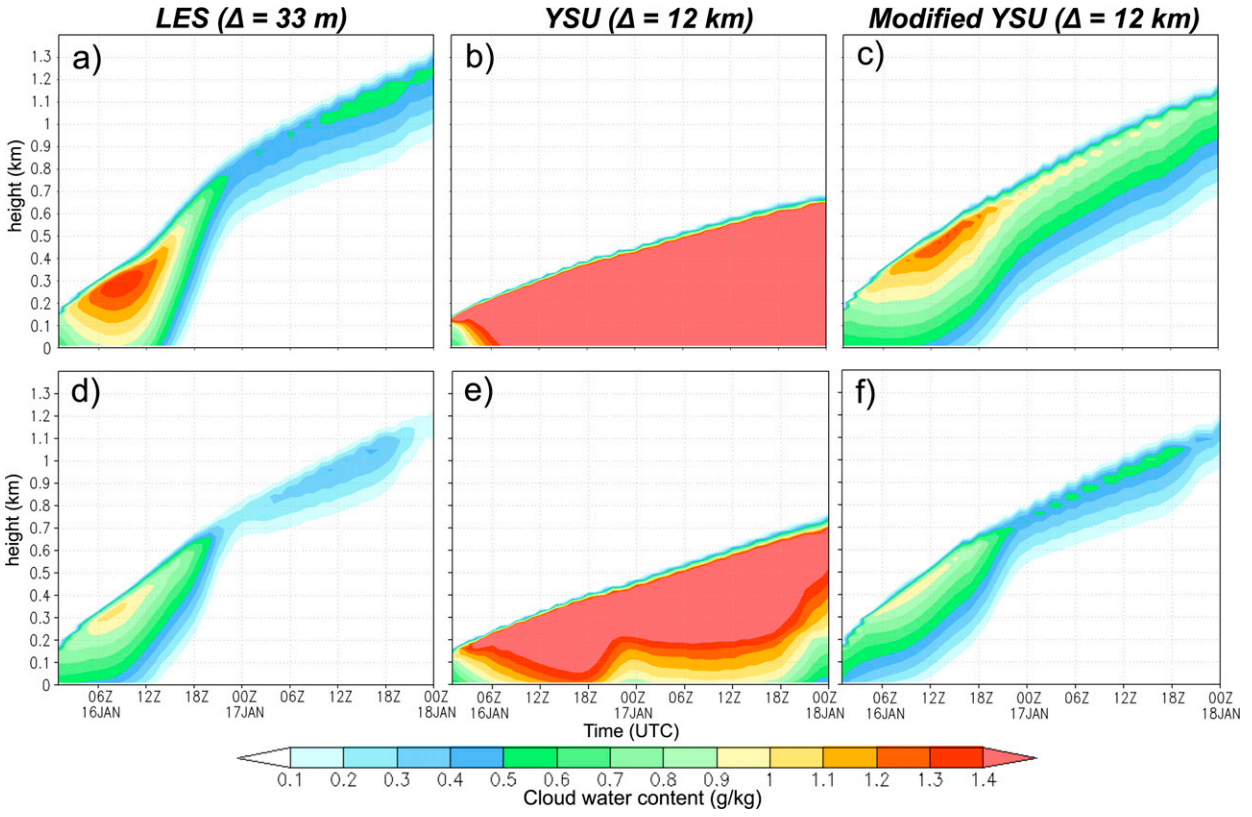

FIG. 5. Domain-average cloud water content (g kg^{-1}) for six 48-h idealized simulations: (a),(d) LES simulations ($\Delta x = \Delta y = 33$ m) with no PBL parameterization, (b),(e) coarse-grid ($\Delta x = \Delta y = 12\,000$ m) standard YSU simulations, and (c),(f) modified YSU ($\Delta x = \Delta y = 12\,000$ m) runs. The original physics setup is used in (a)–(c) whereas altered radiation and LSM schemes are used in (d)–(f). All simulations use 101 vertical levels, with 38 of them within the lowest kilometer. The radiation scheme used a typical CV latitude, longitude, and wintertime solar elevation (16 Jan). See text for additional details.

nonnegligible vertical motions (shaded field in Fig. 6) that developed shortly thereafter. As the fog lifted into stratus, the clouds became less opaque, allowing more shortwave radiation to reach the surface (not shown). Because of this and the continued cloud-top cooling, domain-averaged vertical motions strengthened toward the end of the simulation. It can be seen that vertical motions were largest in the upper portions of the PBL but could extend down near the surface, especially when afternoon heating was active.

These LES results are broadly consistent with previous observational and numerical studies of the nocturnal boundary layer following the development of radiation fog (e.g., Holets and Swanson 1981; Mason 1982; Welch et al. 1986; Boers et al. 2013). For example, in the Welch et al. (1986) results (see also Houze 1993, Fig. 5.3), we note that near-surface temperatures ceased falling in the early morning hours (around 0200 local time), several hours after fog formation but long before sunrise, after which the maximum cooling shifted upward to the top of the foggy layer. During that predawn period, the lapse rates within the fog layer approached (or exceeded) the moist-adiabatic rate. Turbulence responding to the reduced stability was ''directly correlated'' with the increase in the fog-layer depth and liquid water content. Holets and Swanson (1981) noted that in CV fog events the fog layer had a lapse rate between moist and dry adiabatic throughout most of the episode, which is very similar to what is observed in our LES simulation. Additionally, Boers et al. (2013) noted similar atmospheric profiles from radiation fog forming in the Netherlands.

The major difference between the Welch et al. (1986) results and our LES simulation appears to involve the vertical extent of the cloud-topped layer, which in their case only reached 200–300 m. There is some observational support for our significantly deeper fog and stratus layers. Figure 7 presents vertical profiles of equivalent potential temperature θ_e valid at 1600 UTC 1 January 2009 for two San Joaquin valley Radio Acoustic Sounding System (RASS) sites: Chowchilla (CCLCA) and Lost Hills

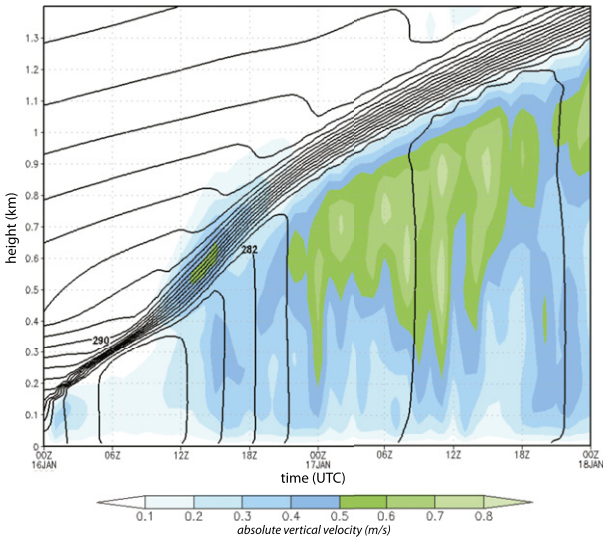

FIG. 6. Domain-average absolute vertical velocity (shaded) and ice–liquid-water potential temperature (contoured) for the LES simulation seen in Fig. 5a.

(LHSCA). RASS provides virtual temperatures before and after correction for vertical air motions (North et al. 1973). Using these data and nearby surface observations, air and vapor pressures and vapor mixing ratios were estimated, presuming that observation levels between 260 and 680 m AGL, inclusive, were saturated. This is a reasonable assumption given that available satellite imagery (not shown) revealed extensive low cloudiness across the SJV, and Fig. 2 indicates that the average valley saturation level was approximately 250 m AGL at this time.[5] The estimated θ_e profiles are close to moist adiabatic in the saturated layer, especially at LHSCA, which is located in the southwestern part of the SJV, where nearby surface observations indicate the fog had not yet lifted.

In pointed contrast, the YSU version of this experiment (Fig. 5b) completely failed to replicate the PBL evolution seen in the LES simulation. This particular run employed the same vertical grid arrangement, model top, SKEBS technique, and doubly periodic horizontal boundary conditions as the LES case, but in a domain that was 120 km on a side with 12-km horizontal grid spacing. Radiation was still called every time step (now 60 s). Note that while the PBL also grew (albeit at a slower rate) through the integration, the fog never lifted from the surface, and the boundary layer cloud content remained quite large. This is in agreement with our real-data case (Fig. 2), in which the YSU simulation unrealistically failed to lift the ceiling substantially throughout the entire simulation, at least when the fog-limiting artificial mixing along model surfaces was deactivated. The physical mechanism through which the LES is able to lift the fog appears to be missing.

We note in passing that the fog and stratus simulated here are likely growing faster than what one would expect in nature for two specific reasons. First, these idealized simulations do not have the synoptic-scale conditions (such as large-scale subsidence) that are often present during the formation of radiation fog/stratus (cf. Underwood et al. 2004). Second, we are running these cases with nothing to oppose the background clear-sky radiational cooling, so the atmosphere in general is cooling more quickly. This allows every point in our sounding (see Fig. 4) to reach saturation more quickly, therefore making the fog "rise" faster. However, since all our idealized simulations are missing subsidence and an opposing heat source to the background radiational cooling, one is still able to compare them directly.

d. *The modified YSU scheme*

The YSU scheme is quite capable of developing realistic mixed layers in response to positive surface heat fluxes (cf. Noh et al. 2003; Hong et al. 2006), but the preceding simulations have identified a clear deficiency in its present implementation. Although our specific focus is on fog, especially the valley fogs that are common in California, the problems at hand bear many similarities to those posed by the stratocumulus-topped PBL. That has been a well-studied topic (e.g., Deardorff 1980; Nicholls and Leighton 1986; Driedonks and Duynkerke 1989; Moeng et al. 1996; Van Meijgaard and Van Ulden 1998) that has provided the authors of this paper with insights into how to fix the fog modeling problem.

In the stratocumulus situation, strong cloud-top cooling may destabilize the boundary layer and drive convective turbulence, even when surface fluxes are negligible (Driedonks and Duynkerke 1989). This represents a form of "top down" mixing, contrasting with the more familiar "bottom up" diffusion associated with surface buoyancy sources (cf. Wyngaard and Brost 1984), and PBL schemes that directly account for top-driven mixing have been proposed and implemented (e.g., Van Meijgaard and Van Ulden 1998; Lock et al. 2000).

[5] The relative humidity (RH) below the saturated layer of the lowest available level was taken to be 90%, consistent with contemporaneous surface reports, and increased linearly with height, while RH was presumed to decrease linearly above 680 m and across the prominent inversion above about 800 m AGL. The true depth of the foggy layer is not known, but these assumptions appear reasonable.

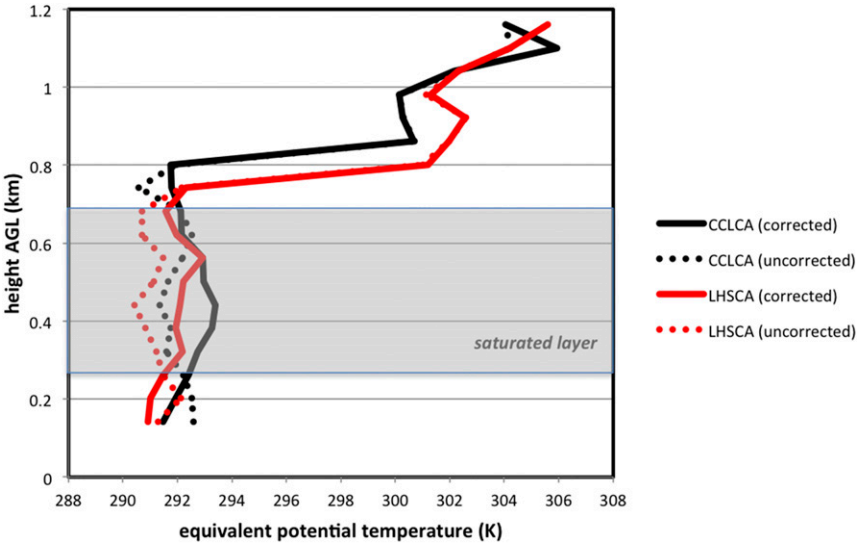

FIG. 7. Vertical profiles of estimated equivalent potential temperature are shown for SJV stations CCLCA and LHSCA, computed from RASS sounder data collected at 1600 UTC 1 Jan 2009, as a function of height AGL. See footnote 5 for additional information.

Although it attempts to account for entrainment across the PBL top from surface thermals, the present version of the YSU is not capable of developing deep-layer diffusion, nor entrainment, specifically in response to a heat sink positioned at the boundary layer top. Therefore, our goal is to modify the YSU scheme to handle the fog and low-stratus problem, without affecting its performance in more conventional convective or stable boundary layers.

The governing equation for the YSU PBL (cf. Hong et al. 2006) is

$$\frac{\partial c}{\partial t} = \frac{\partial}{\partial z}\left[K_c\left(\frac{\partial c}{\partial z} - \gamma_c\right) - \overline{(w'c')}_h\left(\frac{z}{h}\right)^3\right], \qquad (2)$$

where $c = u, v, \theta, q$, the zonal and meridional wind components, potential temperature, and mixing ratio of water vapor, respectively. The geometric height is z, h represents the PBL height, K_c is the eddy diffusivity coefficient, γ_c is the correction to the local gradient reflecting large-scale eddies (the "countergradient term"), and $\overline{(w'c')}_h$ is the flux at the PBL top, which was added to the scheme to accomplish entrainment from surface thermals. Like other K-profile parameterization (KPP) schemes, the eddy mixing as applied to momentum is formulated as (cf. Troen and Mahrt 1986; Hong and Pan 1996)

$$K_m = kw_s z\left(1 - \frac{z}{h}\right)^p, \qquad (3)$$

where k is the von Kármán constant (=0.4), p is the profile shape constant (=2), and w_s is a height-dependent velocity scale that, among other things, is a function of the surface heat flux (Noh et al. 2003). The eddy mixing applied to scalars is related to K_m via the turbulent Prandtl number.

Normalized by w_s and h, (3) yields the prescribed K profile shown by the black curve in Fig. 8. This is the familiar bottom-up mixing profile that has been developed from observations and model simulations (e.g., Businger et al. 1971; Brost and Wyngaard 1978). When the surface layer is stable and surface fluxes are small, however, the diffusion generated by (3) is minimal. Therefore, similar to Van Meijgaard and Van Ulden (1998), we augment this equation with a second term, representing a mixing profile that is similar in shape but that has been reversed and responds to a velocity scale w_{PBL} that is now a function of the PBL top flux rather than the surface fluxes:

$$K_m = kw_s z\left(1 - \frac{z}{h}\right)^p + kw_{\mathrm{PBL}}(h - z)\left(1 - \frac{h - z}{h}\right)^p, \qquad (4)$$

in which

$$w_{\mathrm{PBL}} = \left[ckw_{*h}^3\left(1 - \frac{z}{h}\right)\right]^{1/3}. \qquad (5)$$

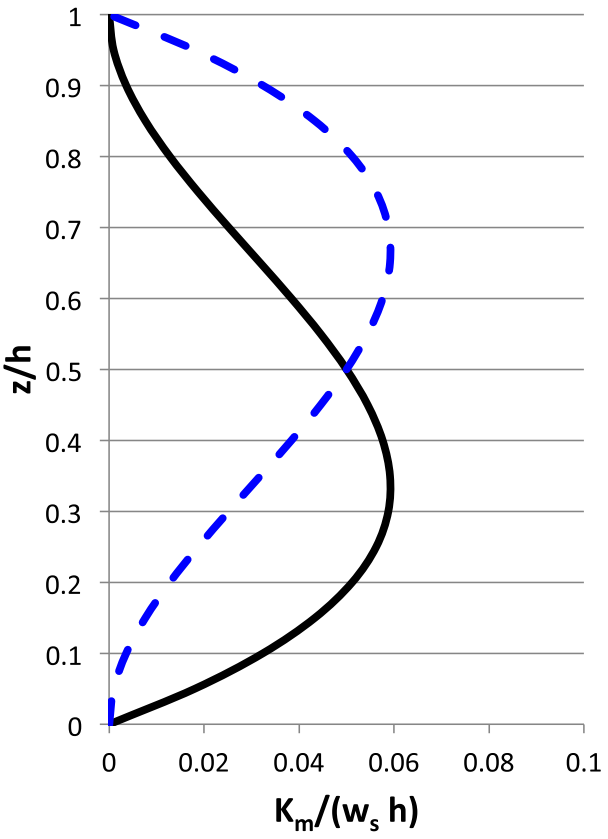

FIG. 8. The prescribed eddy diffusivity profile (black) for the YSU PBL scheme. The second term of the revised eddy diffusivity coefficient [(4)] is shown by the dotted blue line.

In (5), we specify $w_{*h} = [(g/\theta_v)(\overline{w'\theta'_v})_h h)]^{1/3}$ as the convective velocity scale for moist air evaluated at the top of the PBL and, as in the current YSU scheme's w_s, c (=8) is currently held constant.[6]

The boundary layer height in the YSU scheme is identified as the highest level at which the surface-based bulk Richardson number (Rib), formulated as

$$\mathrm{Rib}(z) = \frac{g[\theta_v(z) - \theta_s]z}{\theta_{va} U(z)^2}, \tag{6}$$

becomes less than a selected, stability dependent critical value (Hong et al. 2006). For the boundary layer over land, this value is 0.0 for unstable conditions and 0.25 in stable conditions. In (6), g is the gravitational acceleration; $\theta_v(z)$, θ_s, and θ_{va} are the virtual potential temperatures at height z, the surface, and the first scalar level, respectively; and U is the horizontal wind speed. We have updated (6) to use the ice–liquid-water potential temperature θ_{il}, as the standard formulation would almost always classify a moist-adiabatic profile as stable [since $\theta_v(z) - \theta_s > 0$ in those situations] and would not include it as part of the PBL. With θ_{il}, moist-adiabatic layers can be recognized as being part of the boundary layer, and the PBL top can be more properly placed at the top of the moist-adiabatic layer.

Properly identifying the PBL height is obviously important for calculations like the prescribed K profile in Fig. 8. This alteration also influences the operation of the YSU scheme's entrainment term in (2), as that is evaluated at the diagnosed PBL top. Given a foggy boundary layer with a moist-adiabatic profile, the standard YSU scheme would have likely placed the PBL top somewhere within the moist-adiabatic profile and computing entrainment there would not produce a useful result. However, if one determines the PBL height with θ_{il}, it would be diagnosed at the top of the moist-adiabatic layer, and thus the entrainment term would operate as intended. For completeness and consistency, we have also incorporated the PBL-top heat flux due to radiational cooling from cloud tops $\overline{(w'\theta')}_h$, in the countergradient term, so it becomes

$$\gamma_c = \frac{b}{w_{so} h}\left[\overline{(w'\theta')}_o + \overline{(w'\theta')}_h\right], \tag{7}$$

where $\overline{(w'\theta')}_o$ is the surface thermal flux, b is a coefficient of proportionality, and w_{so} is the mixed-layer velocity at $z = 0.5h$. This was found to have relatively little impact on the results.

Up to this point, the YSU has been given a revised top-down diffusivity coefficient, a revised PBL height calculation by utilizing θ_{il}, and an expanded countergradient term. However, these revisions have not yet added the physics capable of *lifting* a fog layer in our Central Valley simulations. Our analysis suggests that YSU's handling of boundary layer entrainment requires further revision. The standard entrainment term (Hong et al. 2006) is

$$\overline{(w'\theta'_v)}_h = -0.15\left(\frac{\theta_v}{g}\right)\frac{w_m^3}{h}, \tag{8}$$

in which w_m is a velocity scale based on surface fluxes. Even if the inversion layer is properly identified (as discussed above), the entrainment term may be inactive since surface fluxes may be negligible in the foggy boundary layer. Therefore, this term has to be modified to include turbulence generated by cloud-top radiational cooling and evaporative cooling, which have

[6] The most significant difference between (5) and (11)–(12) in Van Meijgaard and Van Ulden (1998) is that we are effectively using a coefficient of $ck = 3.2$ in our velocity scale instead of $c = 1.0$ as in their version. Our formulations differ by what is essentially a tuning parameter, and both should be reconsidered.

been demonstrated to be important in cloud-topped boundary layers such as this (Nicholls and Turton 1986; Shao et al. 1997).

Consequently, a revised entrainment term incorporating a velocity scale based on the PBL-top heat flux w_l was created as

$$\overline{(w'\theta'_v)}_h = -0.15\left(\frac{\theta_v}{g}\right)\frac{w_m^3}{h} - A\left(\frac{\theta_{vh}}{g}\right)\frac{w_l^3}{h}, \tag{9}$$

in which we have

$$w_l^3 = \frac{g\,h}{\theta_h}\frac{I_h}{\rho_h c_p}, \tag{10}$$

$$A = 0.2(1 + a_2 E), \tag{11}$$

and

$$E = \frac{L_v}{c_p}\frac{q_h}{\Pi\Delta\theta_v}. \tag{12}$$

In the PBL-top velocity scale w_l^3, I_h is the radiative flux divergence due to cloud-top cooling while ρ_h is the air density. In addition, A is an entrainment efficiency that, mathematically, can have a minimum value of 0.2, while a_2, the evaporative enhancement coefficient, has been found to be as large as 60 (Nicholls and Turton 1986), although more recent research suggests a value of 15 may be more appropriate (Bretherton et al. 2007; Stevens et al. 2005; Caldwell et al. 2005). As will be shown momentarily, our chosen value of 8 seems to reasonably replicate the entrainment found in our LES simulations. The term E reflects the evaporative enhancement of entrainment (Nicholls and Turton 1986), where $\Delta\theta_v$ is the change in buoyancy across the inversion, and q_h is the cloud water and ice after mixing across the inversion. This added entrainment term acts to decrease the cloud density by allowing drier and warmer air above the inversion to infiltrate the boundary layer. This is in contrast to the revised diffusivity profile, which acts to increase mixing in the PBL. In our simulations, increased mixing replenishes moisture at the top of the PBL and enhances cloud cover, especially over the oceans. Whether the combination of these two terms results in more or fewer clouds is very much dependent on the event and location.

It is important to understand that the changes in the modified YSU scheme are active only under adiabatic conditions capped by clouds. This is because in the dry convective boundary layer, the original YSU scheme has all the physics necessary to do bottom-up mixing and entrainment via surface thermals. Top-down mixing would not be appropriate in dry conditions since there is no heat sink at the top of the PBL. However, in the marine layer and under foggy conditions, we often get a moist-adiabatic profile capped by a cloud (i.e., a heat sink) and that is where our scheme is appropriately activated. To summarize, the PBL depth is first evaluated using (6) but with the ice–liquid-water potential temperature. If a heat sink exists at the top of the PBL, our revised scheme is activated and the top-down mixing [(4)], countergradient [(7)], and entrainment [(9)] terms are recomputed and work in conjunction with the original bottom-up mixing/entrainment. If a heat sink does not exist (as in a cloud-free PBL), the scheme is not activated, and the YSU PBL scheme operates as originally designed.

e. *Testing the modified YSU scheme*

Figure 5c shows the results of the idealized experiment of section 3c above, when the modified YSU scheme is employed. Note that the evolution of the fog and low clouds is more comparable to that seen in the LES simulation (Fig. 5a) in that fog no longer persisted throughout the entire simulation, but rather lifted after the first 18 h. As previously mentioned, the evaporative enhancement coefficient a_2 uses a value of 8 in this case, and in all simulations in this study, to reasonably recreate the LES simulation, although previous research indicates a value near 15 may be more reasonable. Higher values increase entrainment, which in our case, lifted fog too quickly and created less realistic simulations. This suggests there is some uncertainty in the coefficient, and additional research is needed to understand why a 50% reduction in the a_2 coefficient works best to recreate our idealized and real-data simulations. The bottom row in Fig. 5 shows results from still another experiment, with the original sounding, but utilizing the Dudhia/RRTM short- and longwave radiation schemes, respectively, and the five-layer thermal diffusion LSM. The main point of these runs is to demonstrate that the results are not particularly sensitive to specific non-PBL physics choices.

By the end of the original 48-h simulations, the PBL heights in the LES and modified YSU runs (Figs. 5a,c) were just under 1.3 km while it was half that (≈0.6 km) in the original YSU (Fig. 5b) case. These simulations employed 101 model levels, with 38 levels placed in the lowest kilometer. The sensitivity of these results to the vertical and horizontal resolution is presented in Fig. 9. This also assesses the sensitivity to the entrainment rate since, as all simulations were initialized with the same sounding, the PBL height and entrainment are essentially proportional.

Variation of the number of near-surface levels (Fig. 9a) reveals that the modified YSU always produced deeper PBLs than the original version and was always closer to the LES result (indicated by the red triangle), but neither could make use of more than about 40 levels in the lowest kilometer. This is far more than the default number of 8 levels provided by real.exe, and also why we opted to configure the LES with 38 model levels below 1 km. A comparable relationship between PBL height and model levels was also found in our real-case studies (not shown). However, despite these results, our real-data simulations utilize only 19 levels in the lowest kilometer, because this selection is less computationally intensive and less prone to numerical instability.

With respect to horizontal resolution (Fig. 9b), we can note that the original YSU formulation produced deeper PBLs (i.e., had greater entrainment) as the grid spacing was made smaller, but again remained much shallower than in the LES or modified YSU simulations. It is hypothesized that as the horizontal grid was made smaller in the original YSU runs, more turbulence originating near the fog-layer top became resolvable, and thus more entrainment occurred. In other words, when that turbulence remained unresolved, it was not being effectively parameterized in those simulations. In contrast, the modified YSU is far less sensitive to horizontal resolution. We believe this indicates that the parameterized turbulence is properly giving way to resolved-scale mixing as the grid spacing is refined.

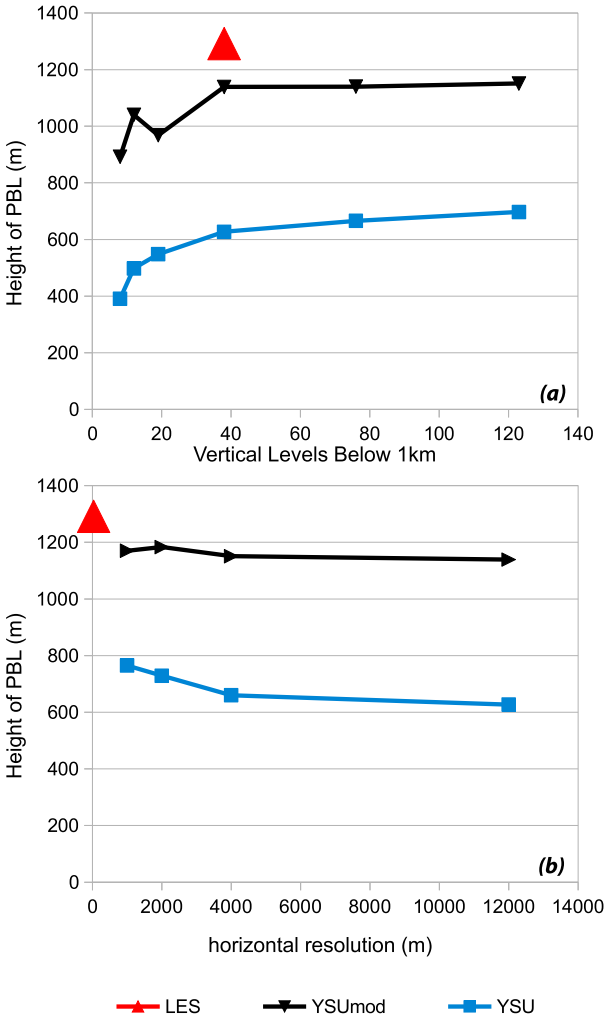

FIG. 9. PBL heights (hour 48) from idealized (a) vertical and (b) horizontal resolution tests are plotted for the YSU (blue) and modified YSU (black) simulations. For reference, the LES simulation result is indicated by the red triangle. Vertical resolution tests use a horizontal resolution of 12 000 m while horizontal resolution tests use a vertical resolution of 101 levels (with 38 levels below 1 km AGL).

f. Case studies

While the modified YSU has performed well in idealized settings, it is necessary not only to demonstrate improvements in real cases but also to show that performance is not degraded in other situations. As previously stated, our modifications are activated only with a cloud-capped moist-adiabatic profile. Figure 10 again focuses on the 29 December 2008–2 January 2009 period examined earlier, now with 4-km horizontal resolution simulations along with the modified YSU results (thick black curves) superimposed. Initially, the two YSU versions yielded very similar reconstructions, which was expected because fog had not yet formed in the SJV. Subsequently, the two simulations diverged, with the modified YSU scheme providing much more accurate forecasts. As occurred in reality, the modified YSU scheme started lifting the ceilings after sunrise on 31 December because it entrained more air into the PBL (as reflected in the warmer 2-m temperatures), while (as noted earlier) ceiling heights continued fluctuating between the first sigma level (18 m), the lowest possible value, and 90 m in the simulation using the original YSU scheme.

Two additional events will be examined, starting with the 13–17 January 2011 period, which included a tule fog episode (Fig. 11). Again, the modified and original YSU runs provided nearly identical reconstructions until the cloud-capped moist-adiabatic layer developed on 14 January. Eventually, the original YSU scheme generated dense fog that it could not lift while the modified version at least managed to produce higher (albeit still too low relative to the observations) ceiling heights that were more realistically modulated by the diurnal cycle. That being said, we also note that the number of forecasted observations with ceilings less than 1000 m in the modified run dipped dramatically during the afternoon

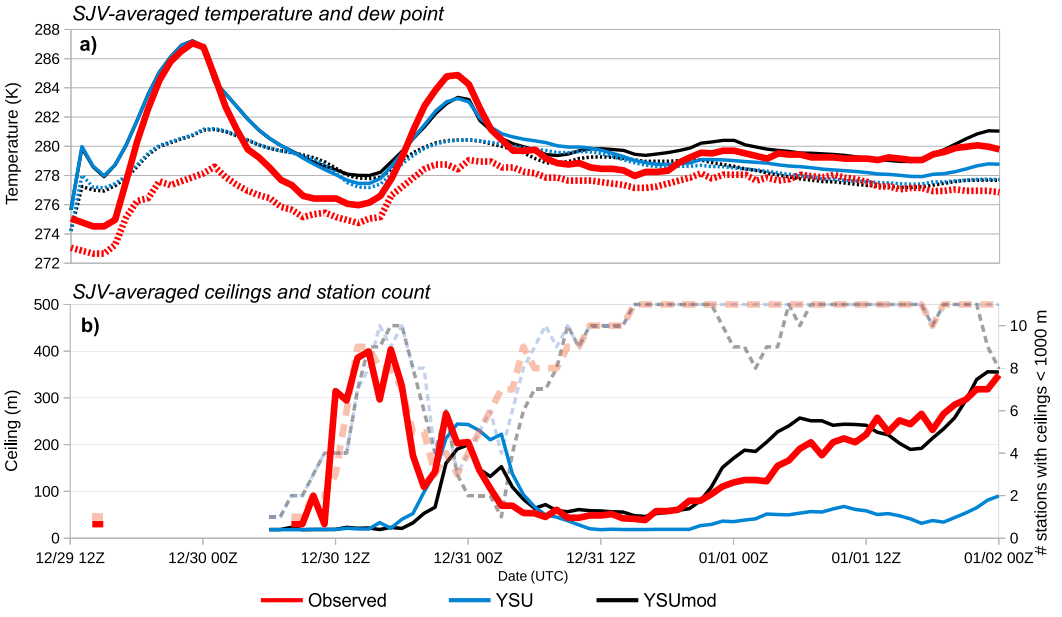

FIG. 10. As in Fig. 2, but with diffusion off, 4-km horizontal resolution, and with the modified YSU scheme added.

hours on 16 and 17 January, but this did not occur in the observations. This may be evidence that the modified YSU scheme is burning off clouds too early, which is perplexing because the average temperature (in this case, from all 10 stations) did not exceed the observed, nor did the ceiling height ever get too high. This may have resulted owing to a model deficiency beyond the PBL itself, including (and not limited to) the microphysics, radiation, the land surface model, and the initialization.

As for the 4–7 January 2011 period (Fig. 12), the original YSU scheme again resulted in an unrealistically prolonged period of very dense fog while our modified version lifted the fog into stratus when that was observed to occur. However, it is also clear that the modified YSU scheme burned off too much of the low clouds on the

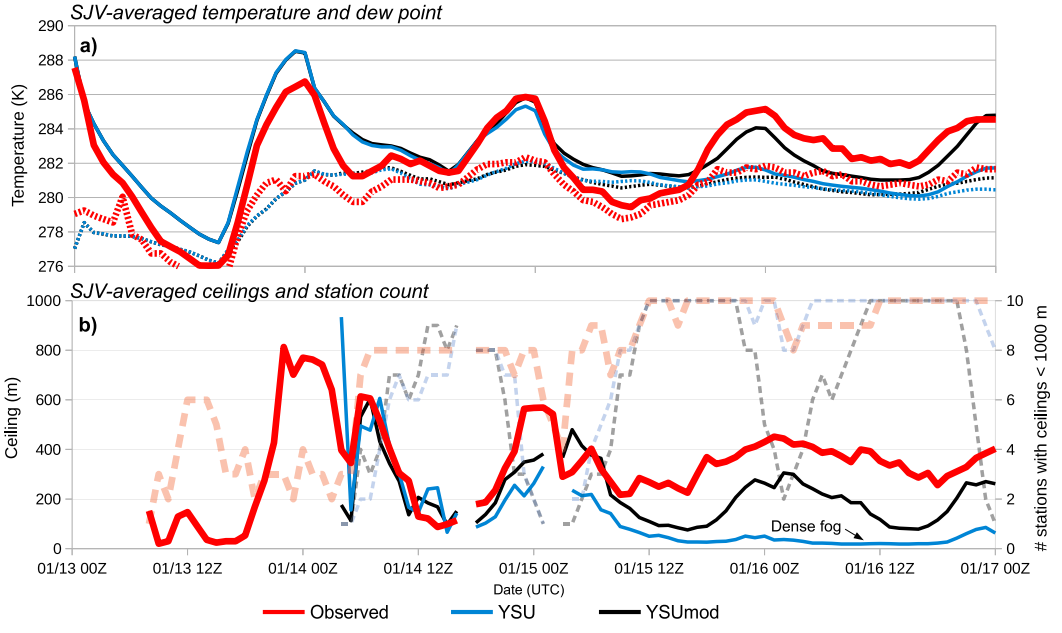

FIG. 11. As in Fig. 10, but for the 13–17 Jan 2011 period.

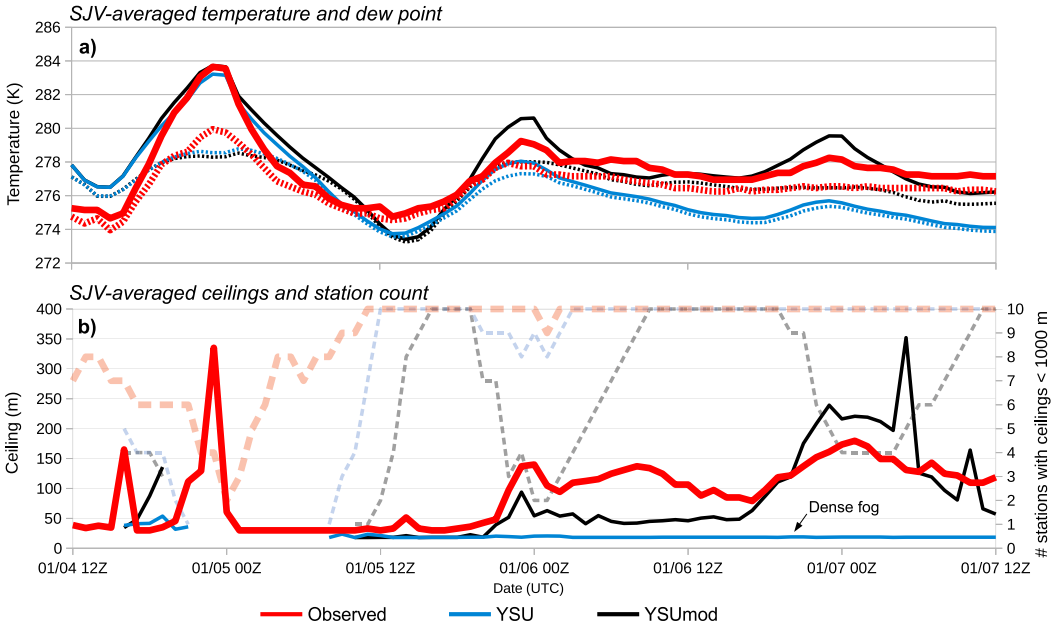

FIG. 12. As in Fig. 10, but for the 4–7 Jan 2011 period.

afternoon and evening of 6 January. Note that, on the evening of 4 January, the number of observed stations reporting fog quickly ramped up after sunset, but the simulations did not start developing fog for another 12 h. Since the fog was later to form, it may also have been too susceptible to burnoff on the next day. In contrast, the original YSU scheme could not mix out the fog, despite the late onset, owing to a lack of entrainment driven by cloud-top fluxes. Thus, in this case the standard YSU scheme appears to be yielding the right answer (in terms of fog coverage) but for the wrong reasons.

It should be noted that in all of these cases, fog formation would have been substantially limited had horizontal diffusion and filters operating along model surfaces not been deactivated. Our modifications to the YSU scheme can be implemented via the WRF namelist switch called ysu_topdown_pblmix, which was added to the model as of version 3.7.

4. Conclusions

California's Central Valley (CV) is home to many urbanized areas that are often subjected to persistent fogs. Forecasting these events has been challenging as a result of missing and/or unphysically parameterized processes. In this paper, it was demonstrated that diffusion operating on model levels, including the WRF Model's sixth-order filter, can completely prevent the formation of fog in even broad valleys, owing to unrealistic transport along mountain slopes. Even coastal fog and low clouds, such as that occurring in southern California, benefited from the reduction in mixing along model levels. This is important as those settings are recommended and thus likely employed by many users who have a need for accurate fog and low-stratus simulations.

Absent horizontal diffusion along model levels, however, we commonly encountered situations in which the fog, once formed in the CV, became unrealistically long lived in simulations made with the YSU PBL scheme. Our analysis led us to realize that the physics necessary to lift fog into low stratus is missing in the default formulation. The problem lies in the fact that the YSU scheme was designed to be a "bottom up" parameterization (cf. Wyngaard and Brost 1984), in that surface fluxes and surface-layer information influence every important process including, but not limited to, the prescribed K profile, the countergradient mixing term, and how entrainment is computed at the PBL top (Hong et al. 2006; Noh et al. 2003). While this may be sufficient for most situations over land, especially for convective boundary layers driven by surface thermals, it was found that an exclusively bottom-up treatment can limit and substantially degrade forecasts when processes are governed by fluxes originating near the PBL top, such as in fog and low-stratus situations.

We have modified the YSU parameterization to include "top down" processes designed to better handle cloud-topped, moist-adiabatic boundary layers, motivated by research into stratocumulus clouds (e.g., Deardorff 1980;

Driedonks and Duynkerke 1989). We added a reversed K profile that is a function of the cloud-top flux to account for thermals originating near the PBL top and augmented the countergradient term to account for the large-scale mixing done by these thermals (although the latter did not have a meaningful impact on the results). More importantly, we added a new entrainment term, controlled by the fluxes at the PBL top, to acknowledge the fact that entrainment is not just a function of surface thermals but also those generated at cloud top by radiative and evaporative cooling. Adopting the ice–liquid-water potential temperature permits more accurate diagnoses of the PBL height under conditions that deviate from dry adiabatic, which is important because without it, the PBL would interpret these conditions as stable and thus incorrectly identify the inversion used in the entrainment calculation. These improvements are activated via a WRF namelist switch, ysu_topdown_pblmix, and designed to alter the results only when and where cloud-capped moist-adiabatic profiles develop.

Through these modifications, we have been able to dramatically improve the ability of WRF to successfully model the evolution and life cycle of fog and low stratus when the YSU PBL scheme is employed, not only for idealized cases but also in real-data forecasts, without degrading its performance in other areas and at other times. It is believe the modified YSU scheme will be of general use to the modeling community and especially to air quality stakeholders and those responsible for transportation facilities.

Acknowledgments. Support for this project was provided by the Developmental Testbed Center (DTC) and San Joaquin Valleywide Air Pollution Study Agency under the management of the California Air Resources Board. The DTC Visitor Program is funded by the National Oceanic and Atmospheric Administration, the National Center for Atmospheric Research, and the National Science Foundation. The authors thank three anonymous reviewers for their constructive comments. This work was derived from material developed for THW's Ph.D. thesis at the University of California, Los Angeles.

REFERENCES

Avey, L., 2011: Challenges of meteorological and photochemical modeling of Utah's wintertime cold pools. Western Meteorological, Emissions, and Air Quality Modeling Workshop, Boulder, CO, Western Regional Air Partnership, https://www.wrapair2.org/pdf/Avey_UT_ColdPolds.pdf.

Baker, K. R., H. Simon, and J. T. Kelly, 2011: Challenges to modeling ''cold pool'' meteorology associated with high pollution episodes. *Environ. Sci. Technol.*, **45**, 7118–7119, https://doi.org/10.1021/es202705v.

Bergot, T., and D. Guedalia, 1994: Numerical forecasting of radiation fog. Part I: Numerical model and sensitivity tests. *Mon. Wea. Rev.*, **122**, 1218–1230, https://doi.org/10.1175/1520-0493(1994)122<1218:NFORFP>2.0.CO;2.

——, E. Terradellas, J. Cuxart, A. Mira, O. Liechti, M. Mueller, and N. W. Nielsen, 2007: Intercomparison of single-column numerical models for the prediction of radiation fog. *J. Appl. Meteor. Climatol.*, **46**, 504–521, https://doi.org/10.1175/JAM2475.1.

Berner, J., S.-Y. Ha, J. P. Hacker, A. Fournier, and C. Snyder, 2011: Model uncertainty in a mesoscale ensemble prediction system: Stochastic versus multiphysics representations. *Mon. Wea. Rev.*, **139**, 1972–1995, https://doi.org/10.1175/2010MWR3595.1.

Betts, A. K., 1973: Non-precipitating cumulus convection and its parameterization. *Quart. J. Roy. Meteor. Soc.*, **99**, 178–196, https://doi.org/10.1002/qj.49709941915.

Billings, B. J., V. Grubišić, and R. D. Borys, 2006: Maintenance of a mountain valley cold pool: A numerical study. *Mon. Wea. Rev.*, **134**, 2266–2278, https://doi.org/10.1175/MWR3180.1.

Boers, R., H. K. Baltink, H. J. Hemink, F. C. Bosveld, and M. Moerman, 2013: Ground-based observations and modeling of the visibility and radar reflectivity in a radiation fog layer. *J. Atmos. Oceanic Technol.*, **30**, 288–300, https://doi.org/10.1175/JTECH-D-12-00081.1.

Bretherton, C. S., P. N. Blossey, and J. Uchida, 2007: Cloud droplet sedimentation, entrainment efficiency, and subtropical stratocumulus albedo. *Geophys. Res. Lett.*, **34**, L03813, doi:10.1029/2006GL027648.

Brost, R. A., and J. C. Wyngaard, 1978: A model study of the stably stratified planetary boundary layer. *J. Atmos. Sci.*, **35**, 1427–1440, https://doi.org/10.1175/1520-0469(1978)035<1427:AMSOTS>2.0.CO;2.

Bryan, G. H., and J. M. Fritsch, 2004: A reevaluation of ice–liquid water potential temperature. *Mon. Wea. Rev.*, **132**, 2421–2431, https://doi.org/10.1175/1520-0493(2004)132<2421:AROIWP>2.0.CO;2.

Businger, J. A., J. C. Wyngaard, Y. Izumi, and E. F. Bradley, 1971: Flux-profile relationships in the atmospheric surface layer. *J. Atmos. Sci.*, **28**, 181–189, https://doi.org/10.1175/1520-0469(1971)028<0181:FPRITA>2.0.CO;2.

Caldwell, P., C. Bretherton, and R. Wood, 2005: Mixed-layer budget analysis of the diurnal cycle of entrainment in SE Pacific stratocumulus. *J. Atmos. Sci.*, **62**, 3775–3791, https://doi.org/10.1175/JAS3561.1.

Chen, F., and Y. Zhang, 2009: On the coupling strength between the land surface and the atmosphere: From viewpoint of surface exchange coefficients. *Geophys. Res. Lett.*, **36**, L10404, doi:10.1029/2009GL037980.

Chou, M.-D., and M. J. Suarez, 1999: A solar radiation parameterization for atmospheric studies. NASA Tech. Memo. TM-1999–104–606, Vol. 15, Goddard Space Flight Center, Greenbelt, MD, 38 pp., https://ntrs.nasa.gov/archive/nasa/casi.ntrs.nasa.gov/19990060930.pdf.

CHP, 2017: SWITRS—Internet statewide integrated traffic records system. California Highway Patrol, https://www.chp.ca.gov/Programs-Services/Services-Information/SWITRS-Internet-Statewide-Integrated-Traffic-Records-System.

Clark, P. A., and W. P. Hopwood, 2001: One-dimensional site-specific forecasting of radiation fog. Part I: Model formulation and idealised sensitivity studies. *Meteor. Appl.*, **8**, 279–286, https://doi.org/10.1017/S1350482701003036.

Deardorff, J. W., 1980: Stratocumulus-capped mixed layers derived from a three-dimensional model. *Bound.-Layer Meteor.*, **18**, 495–527, https://doi.org/10.1007/BF00119502.

Driedonks, A. G. M., and P. G. Duynkerke, 1989: Current problems in the stratocumulus-topped atmospheric boundary layer. *Bound.-Layer Meteor.*, **46**, 275–303, https://doi.org/10.1007/BF00120843.

Ek, M. B., K. E. Mitchell, Y. Lin, E. Rogers, P. Grunmann, V. Koren, G. Gayno, and J. D. Tarpley, 2003: Implementation of Noah land surface model advances in the National Centers for Environmental Prediction operational mesoscale Eta model. *J. Geophys. Res.*, **108**, 8851, https://doi.org/10.1029/2002JD003296.

Federal Aviation Administration, 2010: Weather-related aviation accident study. FAA Rep., 51 pp. + appendixes, http://www.asias.faa.gov/i/2003-2007weatherrelatedaviationaccidentstudy.pdf.

Gustavsson, T., M. Karlsson, J. Bogren, and S. Lindqvist, 1998: Development of temperature patterns during clear nights. *J. Appl. Meteor.*, **37**, 559–571, https://doi.org/10.1175/1520-0450(1998)037<0559:DOTPDC>2.0.CO;2.

Haeffelin, M., and Coauthors, 2010: PARISFOG: Shedding new light on fog physical processes. *Bull. Amer. Meteor. Soc.*, **91**, 767–783, https://doi.org/10.1175/2009BAMS2671.1.

Holets, S., and R. N. Swanson, 1981: High-inversion fog episodes in central California. *J. Appl. Meteor.*, **20**, 890–899, https://doi.org/10.1175/1520-0450(1981)020<0890:HIFEIC>2.0.CO;2.

Holtslag, A. A. M., E. I. F. De Bruijn, and H.-L. Pan, 1990: A high resolution air mass transformation model for short-range weather forecasting. *Mon. Wea. Rev.*, **118**, 1561–1575, https://doi.org/10.1175/1520-0493(1990)118<1561:AHRAMT>2.0.CO;2.

Hong, S.-Y., and H.-L. Pan, 1996: Nonlocal boundary layer vertical diffusion in a medium-range forecast model. *Mon. Wea. Rev.*, **124**, 2322–2339, https://doi.org/10.1175/1520-0493(1996)124<2322:NBLVDI>2.0.CO;2.

——, Y. Noh, and J. Dudhia, 2006: A new vertical diffusion package with an explicit treatment of entrainment processes. *Mon. Wea. Rev.*, **134**, 2318–2341, https://doi.org/10.1175/MWR3199.1.

Houze, R. A., Jr., 1993: *Cloud Dynamics.* Academic Press, 573 pp.

Huang, H., H. Liu, J. Huang, W. Mao, and X. Bi, 2015: Atmospheric boundary layer structure and turbulence during sea fog on the southern China coast. *Mon. Wea. Rev.*, **143**, 1907–1923, https://doi.org/10.1175/MWR-D-14-00207.1.

Kain, J. S., 2004: The Kain–Fritsch convective parameterization: An update. *J. Appl. Meteor.*, **43**, 170–181, https://doi.org/10.1175/1520-0450(2004)043<0170:TKCPAU>2.0.CO;2.

Khairoutdinov, M., and Y. Kogan, 2000: A new cloud physics parameterization in a large-eddy simulation model of marine stratocumulus. *Mon. Wea. Rev.*, **128**, 229–243, https://doi.org/10.1175/1520-0493(2000)128<0229:ANCPPI>2.0.CO;2.

Lim, K.-S. S., and S.-Y. Hong, 2010: Development of an effective double-moment cloud microphysics scheme with prognostic cloud condensation nuclei (CCN) for weather and climate models. *Mon. Wea. Rev.*, **138**, 1587–1612, https://doi.org/10.1175/2009MWR2968.1.

Lock, A. P., A. R. Brown, M. R. Bush, G. M. Martin, and R. N. B. Smith, 2000: A new boundary layer mixing scheme. Part I: Scheme description and single-column model tests. *Mon. Wea. Rev.*, **128**, 3187–3199, https://doi.org/10.1175/1520-0493(2000)128<3187:ANBLMS>2.0.CO;2.

Mason, J., 1982: The physics of radiation fog. *J. Meteor. Soc. Japan*, **60**, 486–498, https://doi.org/10.2151/jmsj1965.60.1_486.

Moeng, C.-H., and Coauthors, 1996: Simulation of a stratocumulus-topped planetary boundary layer: Intercomparison among different numerical codes. *Bull. Amer. Meteor. Soc.*, **77**, 261–278, https://doi.org/10.1175/1520-0477(1996)077<0261:SOASTP>2.0.CO;2.

Nicholls, S., and J. Leighton, 1986: An observational study of the structure of stratiform cloud sheets. Part I: Structure. *Quart. J. Roy. Meteor. Soc.*, **112**, 431–460, https://doi.org/10.1002/qj.49711247209.

——, and J. D. Turton, 1986: An observational study of the structure of stratiform cloud sheets. Part II: Entrainment. *Quart. J. Roy. Meteor. Soc.*, **112**, 461–480, https://doi.org/10.1002/qj.49711247210.

Noh, Y., W. Cheon, S. Hong, and S. Raasch, 2003: Improvement of the K-profile model for the planetary boundary layer based on large eddy simulation data. *Bound.-Layer Meteor.*, **107**, 401–427, https://doi.org/10.1023/A:1022146015946.

North, E. M., A. M. Peterson, and H. D. Parry, 1973: RASS, a remote sensing system for measuring low-level temperature profiles. *Bull. Amer. Meteor. Soc.*, **54**, 912–919, https://doi.org/10.1175/1520-0477(1973)054<0912:RARSSF>2.0.CO;2.

Rao, G.-S., and E. M. Agee, 1996: Large eddy simulation of turbulent flow in a marine convective boundary layer with snow. *J. Atmos. Sci.*, **53**, 86–100, https://doi.org/10.1175/1520-0469(1996)053<0086:LESOTF>2.0.CO;2.

Ryerson, W. R., and J. P. Hacker, 2014: The potential for mesoscale visibility predictions with a multimodel ensemble. *Wea. Forecasting*, **29**, 543–562, https://doi.org/10.1175/WAF-D-13-00067.1.

Shao, Q., D. A. Randall, C. H. Moeng, and R. E. Dickinson, 1997: A method to determine the amounts of cloud-top radiative and evaporative cooling in a stratocumulus-topped boundary layer. *Quart. J. Roy. Meteor. Soc.*, **123**, 2187–2213, https://doi.org/10.1002/qj.49712354403.

Shutts, G., 2005: A kinetic energy backscatter algorithm for use in ensemble prediction systems. *Quart. J. Roy. Meteor. Soc.*, **131**, 3079–3102, https://doi.org/10.1256/qj.04.106.

Skamarock, W. C., and Coauthors, 2008: A description of the Advanced Research WRF version 3. NCAR Tech. Note NCAR/TN-475+STR, 113 pp., http://dx.doi.org/10.5065/D68S4MVH.

Steeneveld, G. J., R. J. Ronda, and A. A. M. Holtslag, 2015: The challenge of forecasting the onset and development of radiation fog using mesoscale atmospheric models. *Bound.-Layer Meteor.*, **154**, 265–289, https://doi.org/10.1007/s10546-014-9973-8.

Stevens, B., and Coauthors, 2005: Evaluation of large-eddy simulations via observations of nocturnal marine stratocumulus. *Mon. Wea. Rev.*, **133**, 1443–1462, https://doi.org/10.1175/MWR2930.1.

Troen, I., and L. Mahrt, 1986: A simple model of the atmospheric boundary layer; sensitivity to surface evaporation. *Bound.-Layer Meteor.*, **37**, 129–148, https://doi.org/10.1007/BF00122760.

Underwood, S. J., G. P. Ellrod, and A. L. Kuhnert, 2004: A multiple-case analysis of nocturnal radiation-fog development in the Central Valley of California utilizing the GOES nighttime fog product. *J. Appl. Meteor.*, **43**, 297–311, https://doi.org/10.1175/1520-0450(2004)043<0297:AMAONR>2.0.CO;2.

Van der Velde, I. R., G. J. Steeneveld, B. G. J. W. Schreur, and A. A. M. Holtslag, 2010: Modeling and forecasting the onset and duration of severe radiation fog under frost conditions. *Mon. Wea. Rev.*, **138**, 4237–4253, https://doi.org/10.1175/2010MWR3427.1.

Van Meijgaard, E., and A. Van Ulden, 1998: A first order mixing–condensation scheme for nocturnal stratocumulus. *Atmos. Res.*, **45**, 253–273, https://doi.org/10.1016/S0169-8095(97)00080-X.

Welch, R. M., M. G. Ravichandran, and S. K. Cox, 1986: Prediction of quasi-periodic oscillations in radiation fogs. Part I: Comparison of

simple similarity approaches. *J. Atmos. Sci.*, **43**, 633–651, https://doi.org/10.1175/1520-0469(1986)043<0633:POQPOI>2.0.CO;2.

Westcott, N. E., 2007: Some aspects of dense fog in the midwestern United States. *Wea. Forecasting*, **22**, 457–465, https://doi.org/10.1175/WAF990.1.

Wilson, T. H., and R. G. Fovell, 2016: Modeling the evolution and life cycle of stable cold pools. *Wea. Forecasting*, **31**, 1753–1769, https://doi.org/10.1175/WAF-D-16-0108.1.

Wyngaard, J. C., and R. A. Brost, 1984: Top-down and bottom-up diffusion of a scalar in the convective boundary layer. *J. Atmos. Sci.*, **41**, 102–112, https://doi.org/10.1175/1520-0469(1984)041<0102:TDABUD>2.0.CO;2.

Xiao, H., and Coauthors, 2015: Modifications to WRF's dynamical core to improve the treatment of moisture for large-eddy simulations. *J. Adv. Model. Earth Syst.*, **7**, 1627–1642, https://doi.org/10.1002/2015MS000532.

Yamaguchi, T., and G. Feingold, 2012: Technical note: Large-eddy simulation of cloudy boundary layer with the Advanced Research WRF model. *J. Adv. Model. Earth Syst.*, **4**, M09003, doi:10.1029/2012MS000164.

Zängl, G., 2005: Formation of extreme cold-air pools in elevated sinkholes: An idealized numerical process study. *Mon. Wea. Rev.*, **133**, 925–941, https://doi.org/10.1175/MWR2895.1.

Zhou, B., and B. S. Ferrier, 2008: Asymptotic analysis of equilibrium in radiation fog. *J. Appl. Meteor. Climatol.*, **47**, 1704–1722, https://doi.org/10.1175/2007JAMC1685.1.

——, and J. Du, 2010: Fog prediction from a multimodel mesoscale ensemble prediction system. *Wea. Forecasting*, **25**, 303–322, https://doi.org/10.1175/2009WAF2222289.1.